Composites Part B 319 (2026) 113688

Contents lists available at ScienceDirect

Composites Part B

journal homepage: www.elsevier.com/locate/composites

# Influence of R-ratio and fracture process zone development on mode II fatigue delamination

Johan Birnie [a,*], Davide Biagini [b], Maria Pia Falaschetti [a], Francisco Monticeli [b], John-Alan Pascoe [b], Enrico Troiani [a]

[a] MaSTeR Lab, Department of Industrial Engineering (DIN), University of Bologna, Via Montaspro 97, Forlì (FC), 47121, Italy
[b] Department of Aerospace Structures and Materials, Faculty of Aerospace Engineering, Delft University of Technology, Kluyverweg 1, 2629 HS, Delft, The Netherlands

ARTICLE INFO

Dataset link: https://doi.org/10.5281/zenodo.18640627

*Keywords:*
Mode II
ELS
Fracture process zone
Fatigue
R-ratio
Delamination
Composite materials

ABSTRACT

Certification of composite structures remains a significant challenge in the aerospace sector. These materials exhibit various failure mechanisms under load, complicating the prediction of crack growth. Delamination is the most common and critical failure, typically triggered by combined tensile and in-plane shear loadings corresponding to Mode I and Mode II, respectively. Characterisation of Mode II remains particularly difficult due to the unstable crack propagation exhibited in many test configurations. This manuscript presents an experimental study of Mode II fatigue delamination at various R-ratios using the End-Loaded Split specimens, which enable stable in-plane shear-driven delamination. A multi-method approach utilising Digital Image Correlation (DIC), Acoustic Emissions, and post-mortem fractography analysis was adopted to provide a comprehensive description of how delamination behaves across varying R-ratios. The study was centred on the fracture process zone, measured via DIC, due to its significant impact on energy dissipation. Variations in the length of this zone throughout the fatigue life revealed an imbalance between the damage mechanisms affecting the growth of the true crack length and the effective crack length. This evolution of the fracture process zone was correlated with trends in acoustic energy dissipation and the morphology of the fracture surface. These findings provide new insights into Mode II fatigue delamination and enhance our understanding for the design of damage-tolerant structures.

## 1. Introduction

Carbon fibre-reinforced polymers (CFRPs) have become increasingly popular in high-performance applications, due to their superior strength-to-weight ratio and design flexibility compared to metals. The aerospace industry in particular has recognised the potential of these materials, as they enable more sustainable flights through significant reductions in structural weight compared to conventional metallic structures. Exemplifying this trend, both the Airbus A350 and the Boeing 787 extensively incorporate composite materials, with composites comprising over 50% of their total weight [1].

Despite their increased use, significant challenges remain. In particular, the understanding of failure mechanisms in composite structures is still under development. Delamination is arguably the most common and critical failure mode in composite laminates, which is caused by high interlaminar stresses [2,3]. This type of damage leads to stiffness degradation and ultimately structural failure.

Real structures typically trigger this type of failure by combining both tensile and in-plane shear loading, referred to as Mode I and Mode II, respectively. While Mode I has been extensively studied in the literature, Mode II has received relatively less attention. The shear-driven nature of the latter presents challenges in establishing a configuration that allows for stable crack propagation, which enables the study and prediction of delamination. This difficulty is also evident in the standardisation of the test configuration. The ASTM standard has adopted the End Notched Flexure (ENF) method for determining Mode II fracture energy [4]. This testing configuration effectively measures fracture initiation values, but it is not suitable for evaluating propagation due to unstable delamination [5,6]. In contrast, ISO has proposed the End Loaded Split (ELS) test configuration [7], which enables stable crack propagation by maintaining the normalised crack length, defined as the ratio of the delamination length to the specimen free length

* Corresponding author.
*E-mail addresses:* johan.birnie2@unibo.it (J. Birnie), d.biagini-1@tudelft.nl (D. Biagini), mariapi.falaschetti2@unibo.it (M.P. Falaschetti), f.m.monticeli@tudelft.nl (F. Monticeli), J.A.Pascoe@tudelft.nl (J.-A. Pascoe), enrico.troiani@unibo.it (E. Troiani).

https://doi.org/10.1016/j.compositesb.2026.113688
Received 21 February 2026; Received in revised form 29 March 2026; Accepted 10 April 2026
Available online 13 April 2026

($a/L$), within a specified range of values [8,9]. The stable crack propagation feature in the ELS makes it highly suitable for studying fatigue delamination growth.

Fatigue loadings pose significant hurdles for certification in the aerospace sector, where a slow-growth approach to design damage-tolerant structures would allow for flying with more efficient structures; however, current structures are still certified with a 'no-growth' philosophy. The Acceptable Means of Compliance (AMC) document AMC 20–29 Composite Aircraft Structure [10] requires engineers to ensure 'slow, stable and predictable' growth if they wish to adopt a slow-growth approach, which is one of the major challenges with composite structures. Understanding how Mode II fatigue crack growth is affected by varying R-ratios is therefore crucial for designing damage-tolerant composite structures.

The R-ratio effect on Mode II delamination has been extensively studied, providing valuable insights into fracture mechanisms and delamination growth models. Research has demonstrated that the R-ratio significantly influences the fatigue threshold and fracture mechanisms in Mode II loading. Post-mortem fractography analyses across different R-ratios reveal changes in surface damage features, including variations in friction effects and microcracking patterns [11–16]. Amaral et al. [16] emphasised the need for a deeper understanding of the fracture process zone (FPZ), given the substantial energy dissipation that occurs within this region. The FPZ refers to the area ahead of the crack tip in which micro-damage mechanisms such as matrix cracking, fibre/matrix debonding, and frictional sliding develop and dissipate energy prior to crack advance [17]. The length of this region during Mode II loading is frequently described as 'large' in the literature [18–21], but how large?

The FPZ can be characterised using Digital Image Correlation (DIC), an optical technique that quantifies surface deformations by correlating the subsequent relative positions of speckles in a pattern applied to the test specimen's surface. DIC has proven highly effective for crack tip monitoring in composites and adhesive bonds, enabling precise localisation of the crack tip by analysing full-field displacement or strain data [22]. Several approaches have been presented in the literature for the development of these tracking algorithms, based on decorrelation [23,24], opening or sliding displacements [25–28], strain distribution [25,29,30], and the equivalent strain energy density (eSED) [31]. An approach combining decorrelation and strain measurements was used in the present work, as the eSED method is more relevant when studying multidirectional laminates, and opening/sliding displacements should only be considered when studying the crack propagation plane.

In addition to DIC, acoustic emission (AE) monitoring, a passive and non-destructive monitoring technology, has proven to be effective in detecting the formation of cracks and damage inside CFRP. When a crack forms, elastic waves propagate through the material and reach the surface, where they are detected by piezoelectric sensors. The acoustic signals are then analysed and can be used to locate damage events, study and characterise damage propagation, and classify damage modes [32]. In the case of fatigue tests, AE data analysis involves additional complications due to friction effects and the larger amount of data to be analysed, making additional filtering strategies necessary. Despite this, several studies have attempted to analyse fatigue delamination propagation in CFRP using AE. Ferreira et al. [33] analysed AE signals within fatigue load cycles at different R-ratios under Mode I loading, providing interesting insights. The R-ratio was observed to influence the damage distribution within a single loading cycle. At low R-ratios, damage events were rarer but more sustained within each cycle. At high R-ratios, instead, more AE activity was detected due to the increased cyclic work applied. Still, each damage event occurred over a shorter time span, as a result of the reduced relative time of the load cycle spent above the threshold for damage propagation. Amaral et al. [16] adopted acoustic emission to characterise energy dissipation at different R-ratios under Mode II loading. By combining information provided by AE and fracture surface analysis, they suggested that, at low stress ratios, increased acoustic emission activity is mainly associated with friction. Conversely, the energy dissipated in the process zone is higher for Mode II delamination at high stress ratios. However, in the previously cited studies, it was not possible to clearly distinguish, using acoustic emissions, between phases of crack coalescence and phases of process zone growth.

The present work aims to increase the understanding of Mode II delamination under fatigue loading, with particular emphasis on R-ratio effects and the role of the fracture process zone. A multi-method approach combining DIC, AE monitoring, and post-mortem fractography analysis is adopted to provide comprehensive insights into the damage mechanisms and failure processes governing shear-driven fatigue delamination.

**Table 1**
Elastic properties of the CFRP T700-DT120 [34,35].

| Properties | Symbol | Value | Units |
|---|---|---|---|
| Longitudinal modulus | $E_{11}$ | 132 | GPa |
| Transverse modulus | $E_{22}$ | 14.5 | GPa |
| Poisson's ratio | $\nu_{12}$ | 0.295 | – |
| Shear modulus | $G_{12}$ | 4.95 | GPa |
| Flexural modulus | $E_{flex}$ | 131.2 | GPa |
| Mode II fracture toughness | $G_{IIC}$ | 2.5 | N/mm |

## 2. Materials and methods

### 2.1. Materials and manufacturing

A unidirectional CFRP prepreg was used, composed of T700 carbon fibre and an epoxy matrix, DT120, from Delta Preg S.p.A (Italy), with an areal weight of 300 g/m$^2$. A laminated panel was manufactured by hand-layup with a $[0_{10}]$ stacking sequence, where an artificial delamination crack of 70 mm was introduced at the mid-plane using a 25 μm-thick Ethylene tetrafluoroethylene (ETFE) film insert. Curing was performed in an autoclave at 135°C for 60 min, under a vacuum of 0.1 bar and a maximum pressure of 6 bar, as recommended by the manufacturer. The main mechanical properties of the laminate are summarised in Table 1 [34,35].

The ELS specimens were cut from the laminate measuring 3.09 ± 0.04 mm in thickness, using a Compcut ACS 600 equipped with a diamond disk, according to the standardised dimensions specified in ISO 15114 [7], i.e. 214 × 20 mm. Additionally, 20 × 15 mm aluminium loading blocks with a central through-hole were bonded to the pre-cracked side on the bottom face with epoxy adhesive. The final dimensions of the specimens are summarised in Table 2 and illustrated in Fig. 1c where $l_{total}$ is the total length of the specimen, $L$ is the free length, $b$ is the specimen's width, and $h$ is the half-thickness. The clamping correction, $\Delta_{clamp}$, was determined during preliminary calibration of the ELS fixture as specified in ISO 15114 [7], where one specimen with a loading block bonded to the end not containing the insert film was loaded to 100 N at different free lengths, obtaining the beam's compliance. The obtained value of $\Delta_{clamp}$ is 15.12 mm [35]. A speckle pattern was applied to the top and side surfaces of each specimen to allow DIC analysis (Fig. 3). All specimens were pre-cracked to a length of approximately 65 mm (visually inspected) under mode I opening to remove any resin-rich regions at the interface between the edge of the film insert and the resin.

### 2.2. Fatigue testing

Eleven specimens were tested under fatigue loading using an MTS 831 Elastomer Test System with a 10 kN load capacity and a 500 N load cell. The tests were conducted under displacement control by applying a sinusoidal waveform at a frequency of 2.5 Hz, with three

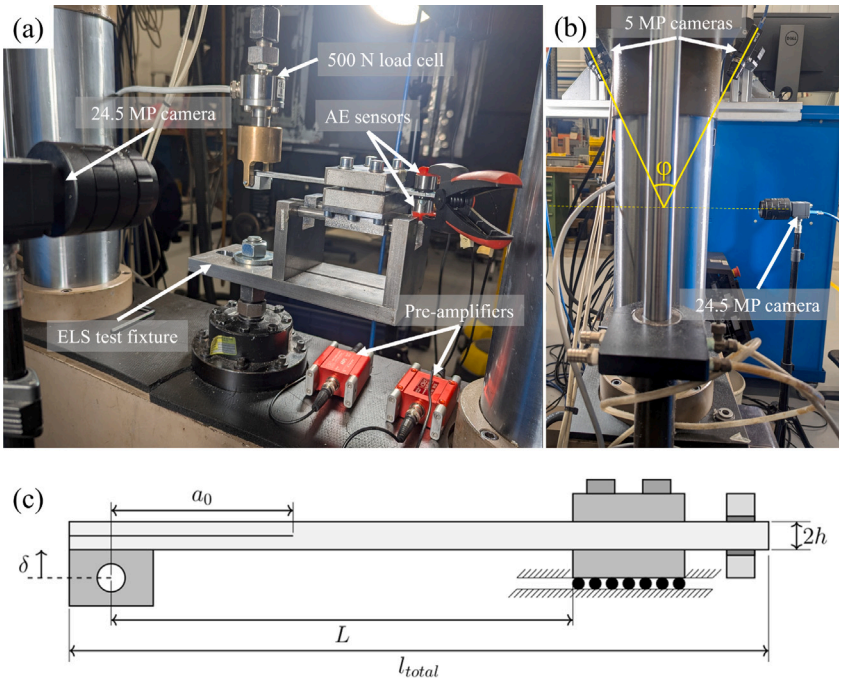


**Fig. 1.** (a) Experimental setup, (b) DIC cameras configuration, (c) illustration of specimen and test scheme.

**Table 2**
Dimensions of ELS specimens.

| Specimen name | $l_{total}$ (mm) | $L$ (mm) | $b$ (mm) | $h$ (mm) |
|---|---|---|---|---|
| ELS_08 | 214.0 ± 0.5 | 105.0 ± 0.5 | 20.22 ± 0.02 | 1.58 ± 0.01 |
| ELS_09 | 214.0 ± 0.5 | 105.0 ± 0.5 | 20.21 ± 0.02 | 1.57 ± 0.01 |
| ELS_10 | 214.0 ± 0.5 | 105.0 ± 0.5 | 20.08 ± 0.02 | 1.57 ± 0.01 |
| ELS_11 | 214.0 ± 0.5 | 105.0 ± 0.5 | 20.10 ± 0.03 | 1.57 ± 0.01 |
| ELS_12 | 214.0 ± 0.5 | 105.0 ± 0.5 | 20.49 ± 0.12 | 1.57 ± 0.01 |
| ELS_13 | 214.0 ± 0.5 | 105.0 ± 0.5 | 19.64 ± 0.21 | 1.56 ± 0.01 |
| ELS_14 | 214.0 ± 0.5 | 105.0 ± 0.5 | 20.41 ± 0.12 | 1.55 ± 0.01 |
| ELS_16 | 213.0 ± 0.5 | 105.0 ± 0.5 | 19.98 ± 0.02 | 1.55 ± 0.01 |
| ELS_18 | 214.0 ± 0.5 | 105.0 ± 0.5 | 20.39 ± 0.02 | 1.52 ± 0.01 |
| ELS_19 | 214.0 ± 0.5 | 105.0 ± 0.5 | 20.40 ± 0.03 | 1.51 ± 0.01 |
| ELS_20 | 214.0 ± 0.5 | 105.0 ± 0.5 | 20.42 ± 0.04 | 1.52 ± 0.01 |

**Table 3**
Overview of the performed fatigue tests.

| Specimen name | $R$ | $\delta_{max}$ (mm) | Number of cycles |
|---|---|---|---|
| ELS_16 | 0.1 | 16.0 | 50,000 |
| ELS_19 | | 16.0 | 50,000 |
| ELS_08 | 0.3 | 22.0 | 7000 |
| ELS_11 | | 18.0 | 30,000 |
| ELS_18 | | 16.0 | 100,270 |
| ELS_13 | | 12.5 | 450,000 |
| ELS_10 | 0.5 | 22.0 | 25,000 |
| ELS_12 | | 18.0 | 184.500 |
| ELS_09 | | 16.0 | 225,580 |
| ELS_20 | | 16.0 | 701,700 |
| ELS_14 | | 12.5 | 701,700 |

displacement ratios ($R$), defined as the ratio between the minimum and maximum displacement ($\delta_{min}/\delta_{max}$), of 0.5, 0.3, and 0.1. The maximum displacement was varied to capture a wide range of energy levels for the same $R$, considering the limited available area for crack propagation caused by the clamp constraint in the ELS fixture. The testing conditions are summarised in Table 3.

Different monitoring techniques were employed during testing, namely Acoustic Emissions (AE) and digital image correlation (DIC): 2D DIC for the side of the specimen and 3D DIC for the top (Fig. 3). The experimental setup is shown in Fig. 1a.

The determination of the fatigue crack propagation rate was simplified during post-processing by fitting a power function for the different crack lengths with respect to the number of cycles. Fitting power functions in this manuscript was conducted using a non-linear least squares regression, with equal weighting, optimised through the Levenberg–Marquardt algorithm to minimise the sum of squared residuals. In contrast, linear fitting was performed using an equally weighted ordinary least squares regression.

The power function used was described in Ref. [36], where the authors concluded that this function reduced scatter with respect to the incremental polynomial method when computing the crack propagation rate and improved the data's fit when compared to other power functions [37]:

$$a = A_1(N + B_1)^{B_2} + A_2 \tag{1}$$

where $a$ is the crack length, $N$ is the number of cycles, $A_1$, $A_2$, $B_1$ and $B_2$ are fitting constants.

Thus, by taking the derivative of Eq. (1), the crack propagation rate $\frac{da}{dN}$ is expressed as:

$$\frac{da}{dN} = A_1 B_2 (N + B_1)^{B_2 - 1} \tag{2}$$

Finally, to determine Paris' Law describing the stable crack propagation region, the following power function was used:

$$\frac{da}{dN} = C_0[f(G)]^m \tag{3}$$

where $C_0$ and $m$ are material constants, and $f(G)$ is a function in terms of the strain energy release (SERR). The material constants were determined after performing a fit of the linearised $\frac{da}{dN}$ and $f(G)$. In this work, $f(G)$ was represented by both the maximum strain energy release rate, $G_{max}$, and the similitude parameter of the cyclic stress amplitude for a general cracked body [14,38], $(\Delta\sqrt{G})^2$, defined as:

$$(\Delta\sqrt{G})^2 = \left(\sqrt{G_{max}} - \sqrt{G_{min}}\right)^2 \tag{4}$$

where $G_{min}$ is the minimum strain energy release rate.

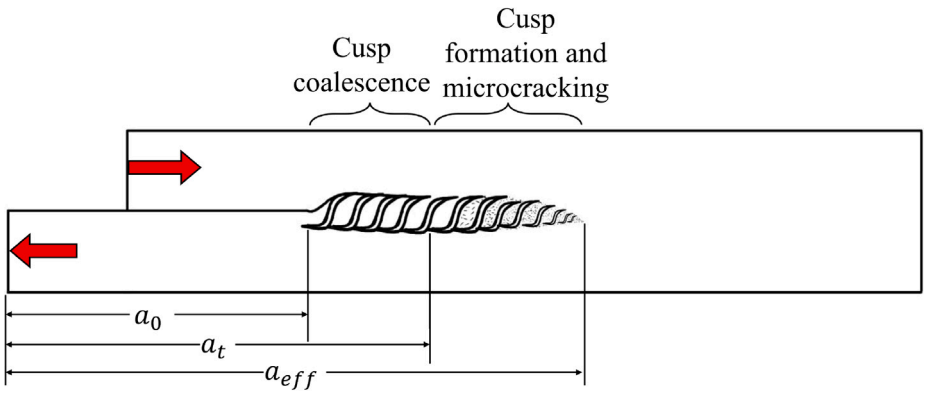


**Fig. 2.** Schematic representation of the initial crack length ($a_0$), true crack length ($a_t$), and effective crack length ($a_{eff}$) in Mode II delamination, indicating regions of cusp coalescence, cusp formation and microcracking.

#### 2.2.1. Data reduction methods

In fracture mechanics, it is important to distinguish between the true crack length, $a_t$, and the effective crack length, $a_{eff}$. The true crack length refers to the position of the physical crack tip, usually identified as the point at which a stress singularity occurs. In practice, $a_t$ is commonly considered as the visible crack tip. In contrast, the effective crack length takes into account additional effects, such as microcracking, bridging and other types of damage near the crack tip, resulting in a position further ahead from $a_t$ (Fig. 2).

This distinction is crucial for Mode II delamination, where there is sliding rather than opening between delaminated surfaces, making direct visual identification of the true crack tip challenging. To overcome this challenge, different methods for determining the effective crack length have been proposed in the scientific literature [8,21,39,40] and are adopted by international standards.

For the determination of the fracture toughness during Mode II delamination, the ISO 15114 test standard recommends three different methods [7]:

- Simple Beam Theory (SBT), based on the beam geometry and material properties:

$$G_{\mathrm{IIC}} = \frac{9P^2a_t^2}{4b^2h^3E_{flex}} \tag{5}$$

  where $P$, is the load.
- Experimental Compliance Method (ECM), based on the cubic relationship between the compliance ($C$) and the true crack length ($a_t$):

$$C = C_i + m_c a_t^3 \tag{6}$$

  where $C = (\delta_{\max} - \delta_{\min})/(P_{\max} - P_{\min})$, $P_{\max}$ and $P_{\min}$ are the maximum and minimum loads, respectively; $m_c$ is the slope of the cubic relationship, and $C_i$ is the compliance before crack propagation. Both $m_c$ and $C_i$ are obtained after performing an ordinary least squares regression. Thus, the fracture toughness is defined as:

$$G_{\mathrm{IIC}} = \frac{3P^2a_t^2m_c}{2b} \tag{7}$$

- Corrected Beam Theory using Effective crack length (CBTE), where the effective crack length is calculated using the measured compliance and the flexural modulus (Eq. (8)), and the fracture toughness is determined as in the SBT (Eq. (9)):

$$a_{eff} = \left[\frac{1}{3}\left\{2bCh^3E_{flex} - (L + \Delta_{clamp})^3\right\}\right]^{\frac{1}{3}} \tag{8}$$

$$G_{\mathrm{IIC}} = \frac{9P^2a_{eff}^2}{4b^2h^3E_{flex}} \tag{9}$$

In this study, only the ECM and CBTE were used. The ECM was demonstrated to output fracture toughness values comparable to those of the CBTE [41]. All calculated values were corrected for large displacement and load-block effects as specified in ISO 15114 [7] and Ref. [8].

### 2.3. Digital Image Correlation (DIC)

Two independent DIC configurations were employed in this analysis to capture deformations from two sides of the specimen: the 2D configuration captured deformations from the side, while the 3D (stereo) configuration captured deformations from the top (Fig. 3).

The 2D DIC system consisted of a 24.5 MP Blackfly S BFS-U3-244S8M-C camera equipped with a 35 mm/F1.8 lens from Edmund Optics. As shown in Fig. 1b, the camera of the 2D DIC system was aligned at the same height as the specimen. The 3D DIC system comprised two 5 MP FLIR GS3-U3-51S5M-C with fitted 23 mm/F1.4 Xenoplan lenses from Schneider. As shown in Fig. 1b, the angle between the two cameras ($\varphi$) was approximately 55°.

Both setups were calibrated prior to testing to ensure proper lighting and optimal specimen focus. Additionally, image acquisition was synchronised with the data acquisition system of the test machine and triggered every 100–1000 cycles.

Data analysis was performed using VIC-2D and VIC-3D software from Correlated Solutions, Inc. for the data obtained from the side and top of the specimen, respectively. The subset size was 31 pixels for all 2D cases, and 29 pixels for the 3D cases. Step size for both configurations was 4 pixels. The results were exported and subsequently post-processed using a Python script.

### 2.4. Acoustic Emissions (AE)

Acoustic emission activity was monitored using two AE sensors positioned after the clamped end of the specimen, as shown in Fig. 1a. Multiple sensors were used to increase the robustness of the measurement. Both sensors were passive broadband piezoelectric VS900-M units from Vallen Systeme GmbH, with an operational frequency range of 100–900 kHz. The signals acquired by the sensors were amplified by 34 dB using two AEP5 pre-amplifiers from Vallen Systeme GmbH. The recorded data were sampled at a 10 MHz frequency with a 50 dB threshold to reduce noise. Furthermore, to guarantee proper coupling between the sensors and the specimen, ultrasound gel was applied.

AE acquisition was performed exclusively for specimens tested at a maximum displacement of 16.0 mm (see Table 3).

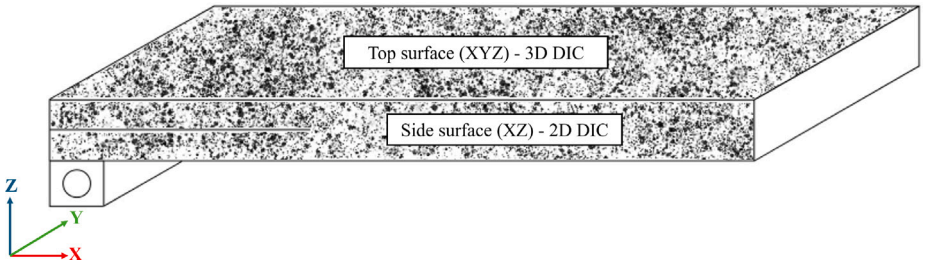


**Fig. 3.** Visual representation of the ELS specimen showing the DIC speckled pattern on the top and side surfaces along the reference coordinate system.

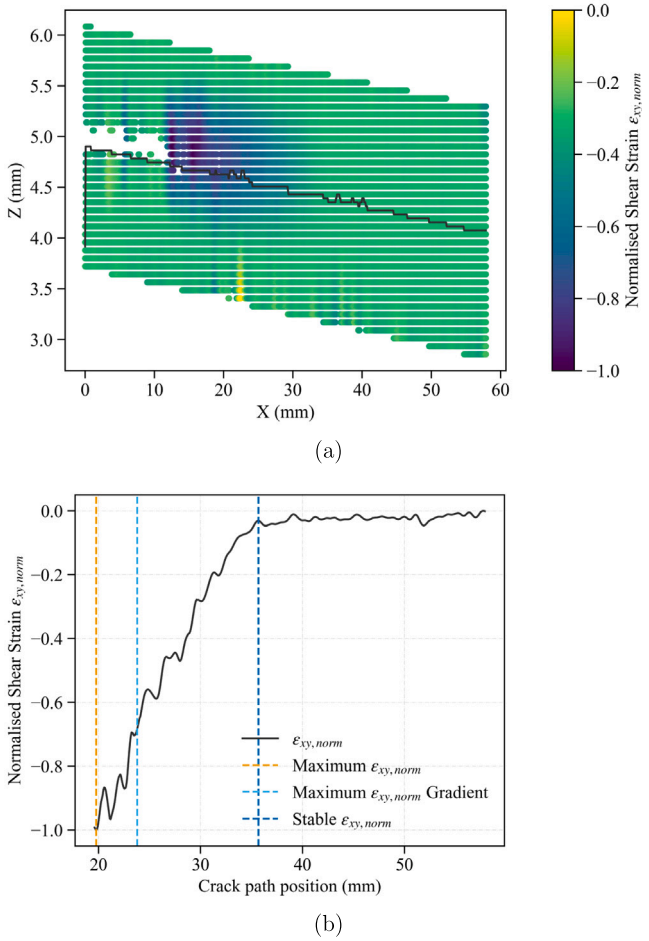


**Fig. 4.** Representative example of (a) Normalised shear strain distribution in the area of interest from DIC outputs, with the mid-plane indicated in black; (b) normalised shear strain distribution along the mid-plane, showing the positions of the identified lengths.

### 2.5. Scanning Electron Microscopy (SEM)

After testing, the fractographic analysis was conducted using a JSM-7500F scanning electron microscope (SEM). Prior to observation, representative areas of the fracture surfaces were cut into smaller coupons and sputter-coated with a thin gold layer of approximately 15 nm to ensure adequate electrical conductivity and image quality. One representative specimen from each R-ratio was selected to examine potential morphological differences in the fracture features. The image acquisition was performed at magnifications of 250× and 500×, using an acceleration voltage of 5 keV and a beam current of 10 mA. The working distance during imaging was maintained at approximately 14.5 mm, optimised to achieve a balance between image resolution and depth of field.

## 3. Results and discussion

### 3.1. Crack propagation monitoring

Output variables from the DIC analysis were utilised in an algorithm developed in Python for the identification of the true and effective crack lengths. For each analysed loading cycle, the specimen's positional data, strain measurements, and sigma values (correlation coefficient, indicating the standard deviation and confidence in the match) were considered. Analyses from the top and side of the specimen are described in detail in the following sections.

#### 3.1.1. Side surface - 2D DIC

Using a side-view configuration, 2D DIC enabled the analysis of deformations on a single observation plane aligned with the specimen's through-thickness direction (XZ plane, see Fig. 3). In a Mode II strain-based analysis, from this perspective, shear strains are predominantly observed in the vicinity of the mid-plane during delamination (Fig. 4a). Therefore, the shear strains ($\varepsilon_{xy}$) at the mid-plane, which corresponds to the crack propagation path, were extracted for further analysis.

Decorrelation may indicate that a fracture has occurred at the analysed point [23]. The parameter sigma can be useful in identifying decorrelation, as it indicates the accuracy of the computed deformations. Hence, high sigma values may suggest that a fracture has taken place even without complete decorrelation. To avoid misidentifying the true crack length, filtering was performed by identifying a series of consecutive points that exceeded a calibrated sigma threshold of 4.6%. The threshold was determined through an iterative calibration procedure aimed at minimising noise in the strain data before the minimum strain.

As demonstrated by Corleto et al. [42], in the proximity of the crack tip, there is a high concentration of shear stresses that decrease monotonically to a constant value. In the analysed cases, identifying the maximum concentration of shear strain from the DIC measurements may result in misplacing the location of the crack tip due to fibre bridging, as discussed by Tu et al. [31], which plays an important role in Mode II delamination. This phenomenon can affect the strain distribution near the crack tip, as demonstrated by Massabo and Cox [43], and the influence of friction in the vicinity of the crack tip, as discussed by Amaral et al. [16]. Therefore, the point of maximum shear strain gradient, after smoothing the strain in the region of interest to prevent data-noise interference, was selected as the most probable indicator of the true crack length, similarly to the method presented by Tu et al. [31], which delimited the high strain gradient region.

The effective crack length, on the other hand, was identified as the point ahead of the true crack length, where shear strains become stable again, indicating the end of the FPZ as described in Ref. [44]. The identified strains in the mid-plane are exemplified in Fig. 4b.

### 3.1.2. Top surface - 3D DIC

Unlike the 2D analysis, which captures deformations within a single plane, the 3D (stereo) DIC provides full-field, three-dimensional deformation measurements from the top surface of the specimen. During the ELS test, the specimen undergoes constrained bending to induce Mode II sliding in the mid-plane, resulting in an out-of-plane motion; under these circumstances, a 2D DIC analysis from the top of the specimen cannot provide reliable deformation measurements. As the bent specimen primarily experiences longitudinal stresses, the longitudinal strains ($\epsilon_{xx}$) were considered in this analysis (Fig. 5a).

In this case, the crack is not directly identified, but the distribution of strains on the top surface indicates the locations of both the true and effective crack lengths. The true crack length is associated with the point where the bending moment, and thus the longitudinal strain, reaches its maximum value. Similar to the shear strain analysis on the specimen's side, the effective crack length is identified as the point at which the strains return to a stable value.

This method has been employed in the literature for crack propagation monitoring with optical fibre sensors placed on the top or bottom surfaces of a specimen [45–48]. Similarly to the positioning of optical fibre sensors on the surface of a specimen, the longitudinal strain distribution from the DIC data was divided into 50 slices along the specimen's width, within which the true and effective crack lengths were identified (Fig. 5b). This technique provided insights into crack front lengths. To facilitate monitoring of crack propagation, the mean value of these front lengths was computed as a reference (Fig. 5c).

### 3.1.3. Estimated true and effective crack lengths from DIC

The results from the monitoring algorithm from both the specimen's side and top measurements, compared with the calculated effective crack length (Eq. (8)), are presented as a function of the number of fatigue cycles in Fig. 6.

Monitoring of the effective crack length using both 2D and 3D DIC methods captures the trend of the calculated one, although evident differences arise in some cases. In certain specimens (e.g. ELS_08, ELS_11, ELS_16, ELS_19), the calculated effective crack length exceeds the clamp limit, suggesting that microcracking and cusp formation may continue beyond the clamp. This could not be confirmed by the DIC measurements because the area was outside the region of interest; moreover, the clamp also acts as a crack-arrest feature, so delamination cracks are not expected to initiate or propagate beyond this point. As the crack approaches the clamp, delamination propagation stops, and the dominant fatigue damage mechanism may shift to another mode, as the specimen remains subjected to cyclic bending, which causes an increase in compliance. Additionally, the 3D DIC measurements of $a_{eff}$ become less reliable near the clamp due to the sharp transition between the clamp and the specimen; in this region, the painted speckle pattern tended to deform more, resulting in unreliable strain measurements, as seen in Fig. 5a, where there is a non-uniform strain distribution near the clamp (X ≈ 80 mm).

Monitoring of the true crack length using 2D DIC measurements presented certain challenges as highlighted in Section 3.1.1. Moreover, on the specimen's side, cusp formation can lead to detachment of the speckled pattern paint, resulting in unreliable DIC measurements in this region.

To address the limitations of both 2D and 3D DIC measurements, the true crack length obtained from the top of the specimen and the effective crack length from the side were considered. These measurements were deemed the most reliable and least noisy with respect to the test setup.

### 3.1.4. Estimation of fracture process zone

The fracture process zone was estimated by calculating the difference between the effective and true crack lengths:

$$l_{FPZ} = a_{eff} - a_t \tag{10}$$

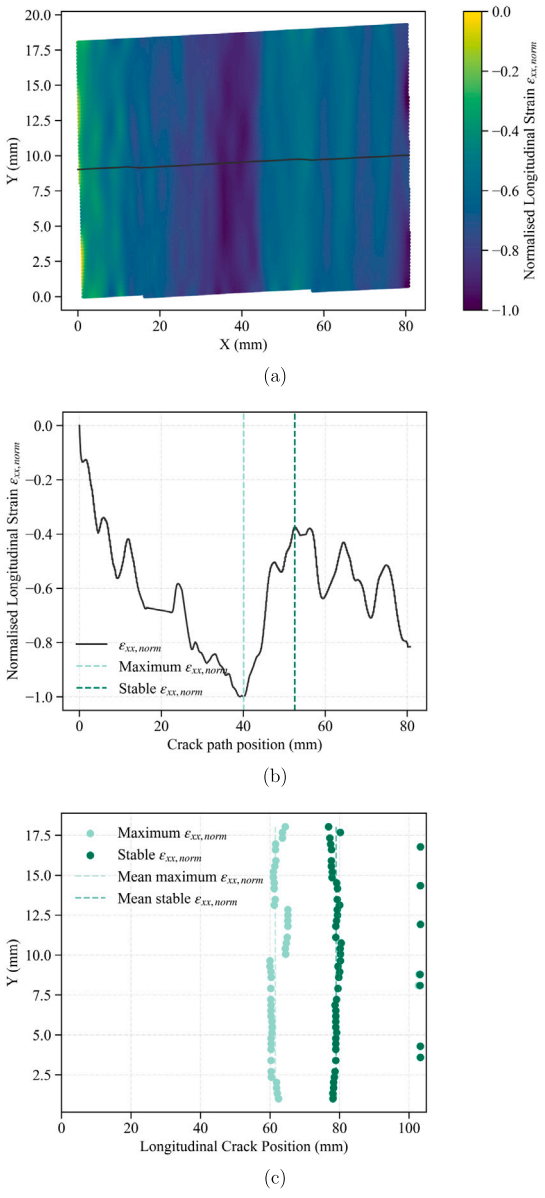


**Fig. 5.** Representative example of (a) Normalised longitudinal strain distribution in the area of interest from DIC outputs; (b) normalised shear strain distribution along a longitudinal slice, showing the positions of the identified lengths; (c) true and effective crack lengths distributed along the width of the specimen with their respective mean values.

Fig. 7 shows the fracture process zone length as a function of the effective crack length and number of cycles. It is important to note that during fatigue, $l_{FPZ}$ is not constant; it varies as delamination propagates. This variation arises from the distinct fracture mechanisms active in Mode II, including microcracking, cusp formation, and cusp coalescence. Microcracking and cusp formation occur within the FPZ and contribute to its gradual extension ahead of the visible crack tip, as reflected by the effective crack length (Fig. 6). However, when these damage features coalesce, the delamination front advances abruptly towards the leading edge of the FPZ, referred to as 'crack jumps' [16]. As a result, significant variations in the apparent FPZ length are seen following each coalescence event. Hence, a constant, fully developed FPZ is infrequently observed during Mode II fatigue crack growth.

While a complete description of the crack jump pattern is prevented due to having insufficient evidence, certain observations emerge. Comparison of the maximum FPZ length against the maximum applied

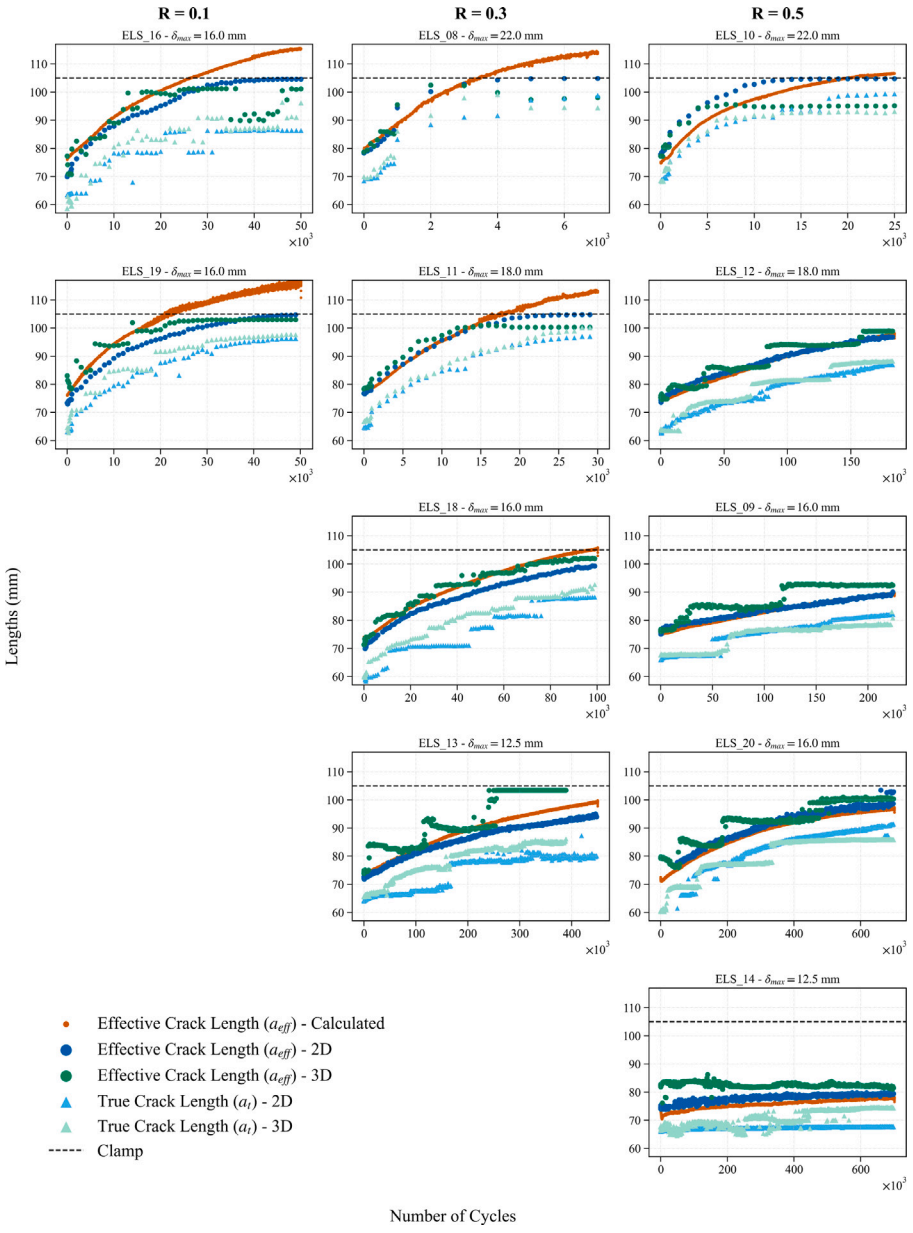


**Fig. 6.** Comparison of the effective crack length and true crack length (measured via 2D and 3D DIC) and calculated effective crack length versus the number of fatigue cycles at different displacement ratios divided by R-ratio.

displacement reveals consistent behaviour across specimens. For instance, specimens subjected to a maximum applied displacement of 16.0 mm (excluding ELS_20) exhibit a maximum FPZ length of approximately 12 mm. The maximum stress at the cusps is equal across all specimens, and the maximum length of the FPZ describes a critical state at which unstable cusp coalescence takes place, triggering a crack jump.

The rate of FPZ development during fatigue appears to depend on the stage of the specimen's fatigue life (Fig. 7). In the early stages, when energy dissipation is higher, the FPZ reaches its critical length more rapidly with respect to the successive crack jumps, which take place after a higher number of cycles. At lower R-ratios or higher maximum displacements (conditions associated with greater energy dissipation per cycle), the variation in $l_{FPZ}$ is reduced, indicating more consistent FPZ and true crack length development. Conversely, at higher R-ratio or lower maximum displacement (associated with lower energy dissipation), the amplitude of FPZ variation increases. For example, comparing ELS_11 ($R = 0.3$) and ELS_12 ($R = 0.5$), having the same maximum displacement, it is observed that at a higher R-ratio, the variation in $l_{FPZ}$ is greater, but it takes longer to reach the critical state. The described behaviour suggests that the FPZ during fatigue is influenced by both the maximum displacement and R-ratio, as evidenced by the occurrence of crack jumps.

Another comparison method may be achieved by fixing the initial strain energy release rate or severity (ratio between maximum SERR and fracture toughness, $G_{\max}/G_C$), therefore fixing the maximum displacement accordingly. This approach would require strict control of the specimen's pre-cracking, which is particularly challenging in shear-dominated delamination, given that small variations in the initial crack length directly affect the initial energy level.

An energy-controlled testing approach, where the maximum strain energy release rate (SERR) is kept constant, as proposed by Allegri et al. [49], represents a potential alternative for achieving stable delamination growth. However, its implementation requires automated crack length monitoring and may involve extensive experimental efforts to determine Paris' law parameters.

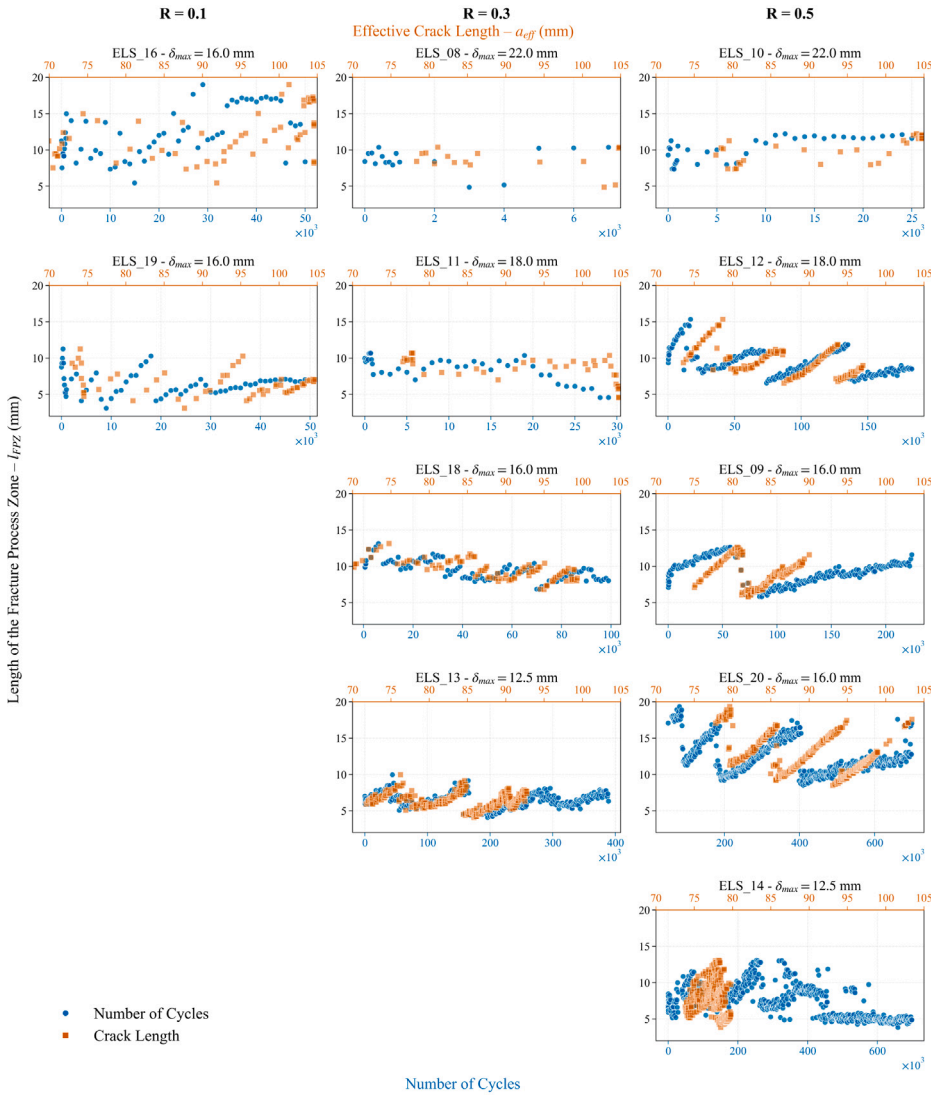


**Fig. 7.** Length of the fracture process zone ($l_{FPZ}$) determined by combining 2D and 3D DIC data as a function of effective crack length (orange axis) and number of cycles (blue axis) divided by R-ratio. (For interpretation of the references to colour in this figure legend, the reader is referred to the web version of this article.)

Although not considered in the present study, these approaches offer a relevant framework for future investigations on the influence of initial damage severity and R-ratio on the fracture process zone.

### 3.2. Fatigue crack propagation

The crack propagation rate was evaluated for both $a_{eff}$ and $a_t$ using the power-law fitting approach described in Eqs. (1) and (2). As previously discussed, $a_t$ exhibits frequent crack jumps, which lead to a sudden increase in the immediate crack propagation rate. However, the adopted fitting procedure inherently smooths out these events. Consequently, the crack propagation rate does not capture these abrupt changes; instead, it is reflected in the immediate variations of the SERR.

As the specimens were tested at various maximum displacements, delamination occurred at different energy levels, allowing to plot a single Paris curve that contains a broad range of energy levels per displacement ratio. For each displacement ratio, a single curve was fitted (see Eq. (3)). The fitting was performed on the region where stable crack propagation was identified.

Regarding the maximum strain energy release rate ($G_{\max}$), the Paris' law curves considering $a_{eff}$ are depicted in Fig. 8a, and in Fig. 8b those considering $a_t$. The resulting Paris' Law curves for both effective and true crack lengths are directly compared in Fig. 8c, and their coefficients are listed in Table 4. All the curves presented a high coefficient of correlation ($R^2 > 0.85$), highlighting the good quality of the fit and the data. Greater dispersion is observed for $a_t$ at $R = 0.1$ because tests at this R-ratio were shorter. The reduced fatigue life places more emphasis on the initiation and early crack propagation stages, where higher energy levels are associated with rapid growth. Consequently, this results in fewer data points and, inherently, greater scatter.

For $R = 0.1$, the difference between the effective and true crack length Paris' curves is small, with the $m$ coefficient differing by 2.599%. At this low R-ratio, as highlighted in the preceding section, the FPZ exhibits small variation, indicating that microcracking and cusp formation progress at comparable rates relative to cusp coalescence. The obtained Paris' curves sustain this hypothesis. This balanced damage progression, as observed in [16], can be attributed to the crack closure effect, which generates higher friction between cusps, triggering coalescence and formation at a similar rate and also generating a more worn fracture surface. The post-mortem fractography analysis is discussed in detail in Section 3.4.

For $R = 0.3$ and $R = 0.5$, more substantial differences emerge between the Paris' law curves for effective and true crack lengths, with

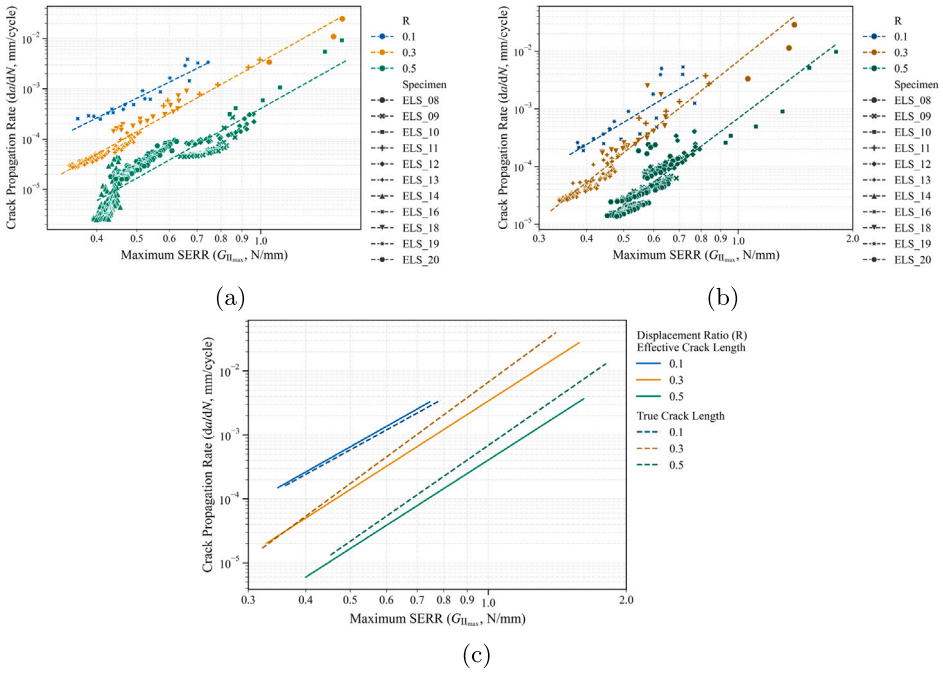


**Fig. 8.** Mode II fatigue crack propagation rate as a function of the maximum SERR, (a) using the effective crack length, (b) using the true crack length, (c) all specimens grouped by R-ratio, effective and true crack length (merged curves).

**Table 4**
Paris' law coefficients from maximum SERR curves comparing results obtained with both true and effective crack length across different displacement ratios, with their respective coefficient of determination ($R^2$) and the relative percentage difference of $m$ (Error).

| $R$ | | $C_0$ | $m$ | $R^2$ | Error (%) |
|---|---|---|---|---|---|
| 0.1 | $a_{eff}$ | $1.080 \times 10^{-2}$ | 4.053 | 0.954 | 2.599 |
| | $a_t$ | $8.998 \times 10^{-3}$ | 3.949 | 0.808 | |
| 0.3 | $a_{eff}$ | $3.393 \times 10^{-3}$ | 4.601 | 0.975 | 13.496 |
| | $a_t$ | $6.680 \times 10^{-3}$ | 5.267 | 0.961 | |
| 0.5 | $a_{eff}$ | $4.049 \times 10^{-4}$ | 4.604 | 0.890 | 7.946 |
| | $a_t$ | $6.858 \times 10^{-4}$ | 4.985 | 0.910 | |

**Table 5**
Paris' law coefficients from the similitude parameter $(\Delta\sqrt{G})^2$ curves comparing results obtained with both true and effective crack length across different displacement ratios, with their respective coefficient of determination ($R^2$) and the relative percentage difference of $m$ (Error).

| $R$ | | $C_0$ | $m$ | $R^2$ | Error (%) |
|---|---|---|---|---|---|
| 0.1 | $a_{eff}$ | $2.536 \times 10^{-2}$ | 4.053 | 0.954 | 2.599 |
| | $a_t$ | $2.068 \times 10^{-2}$ | 3.949 | 0.809 | |
| 0.3 | $a_{eff}$ | $4.962 \times 10^{-2}$ | 3.882 | 0.988 | 16.682 |
| | $a_t$ | $1.475 \times 10^{-1}$ | 4.589 | 0.928 | |
| 0.5 | $a_{eff}$ | $2.045 \times 10^{-1}$ | 4.528 | 0.882 | 9.977 |
| | $a_t$ | $7.013 \times 10^{-1}$ | 5.003 | 0.886 | |

the $m$ coefficient differing by 13.496% and 7.946%, respectively. This variation reflects the disparate rates at which the failure mechanisms active in Mode II progress. In these cases, microcracking and cusp formation proceed at markedly higher rates than cusp coalescence. This imbalance in the progression of the damage mechanisms triggers noticeable crack jumps, which manifest marked oscillatory variations in the FPZ length during fatigue. Consequently, the FPZ exhibits greater variability compared to the low R-ratio case. Additionally, at these R-ratios, crack closure effects are reduced, diminishing the role of friction between cusp surfaces. As a result, damage features on the fractured surfaces become more prominent, indicating that energy dissipation is concentrated in the active FPZ rather than dissipated through frictional sliding.

For $(\Delta\sqrt{G})^2$, the Paris' law curves considering $a_{eff}$ are depicted in Fig. 9a, and in Fig. 9b those considering $a_t$. The resulting Paris' Law curves for both effective and true crack lengths were directly compared in Fig. 9c, and their coefficients are described in Table 5.

The crack propagation using $(\Delta\sqrt{G})^2$ generally exhibits the same behaviour as that described using $G_{\max}$. A significant observation emerges when comparing the crack propagation behaviour between $a_{eff}$ and $a_t$: in Fig. 9a, the curves from different R-ratios tend to collapse together into a single one, as expected when describing the Paris Law with the similitude parameter $(\Delta\sqrt{G})^2$. In contrast, in Fig. 9b, the curves are more dispersed, with variations of up to 16.682% across different R-ratios. This dispersion reflects the various damage mechanisms occurring for $a_t$ at different R-ratios, namely cusp coalescence, friction, and the crack jumps.

### 3.3. Acoustic emissions

As detailed in the methodology section, AE signals were recorded by two sensors positioned beyond the clamped region, equidistant from the crack front on the top and bottom faces of the specimen. This configuration allowed localisation to filter acoustic signals originating from damage propagation, focusing exclusively on waveforms that reach both sensors simultaneously, with a time delay of less than 0.001 ms.

The signals were analysed in terms of AE energy release at different R-ratios and correlated with the evolution of the fracture process zone length, determined via DIC as described in the previous sections. Figs. 10, 11, and 12 present these data against the fatigue life fraction (normalised cycles) for $R = 0.1$, 0.3, and 0.5, respectively. Across all R-ratios, AE energy release occurs in distinct phases of high and low activity rather than at a constant rate, consistent with intermittent crack jump behaviour.

Comparing the released energy with the evolution of the process zone reveals clear R-ratio-dependent patterns. For $R = 0.1$, no evident increasing trend in the process zone is observed. This is also reflected in

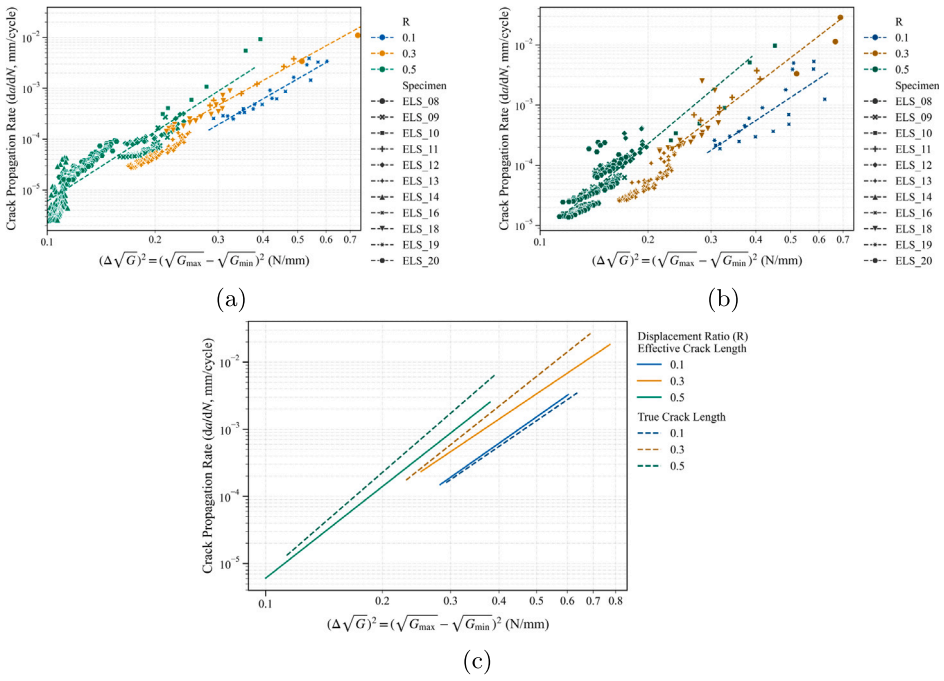


**Fig. 9.** Mode II fatigue crack propagation rate as a function of the similitude parameter $(\Delta\sqrt{G})^2$, (a) using the effective crack length, (b) using the true crack length, (c) all specimens grouped by R-ratio, effective and true crack length (merged curves).

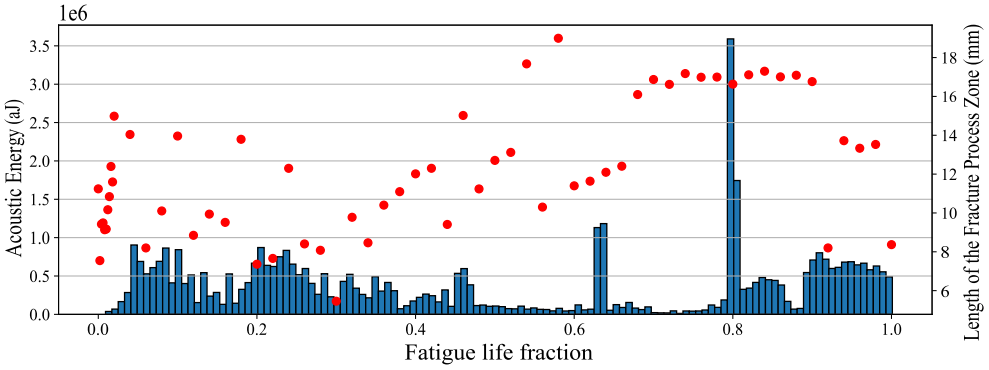


**Fig. 10.** Histogram for release of acoustic energy (left axis) during fatigue test at $R = 0.1$ compared with the process zone length evaluated with DIC (red circles, right axis).

the acoustic energy release, which alternates between peaks and valleys without a clear trend. In contrast, for $R = 0.3$ and $R = 0.5$, distinct phases of process-zone growth, as detected using the DIC method, are accompanied by a gradual increase in acoustic emission activity. This is particularly evident in the final stage of the $R = 0.3$ (Fig. 11) test and throughout the $R = 0.5$ test (Fig. 12). An increase in released acoustic energy per test segment is representative of either an increase in the scale of damage (i.e., higher energy per event in a statistical sense), an increase in the number of events per segment (i.e., more damage per unit time), or a combination of both. This pattern could indicate that the initial process-zone growth phase is characterised by local damage mechanisms such as micro-cracking and fibre–matrix debonding, generating relatively low levels of acoustic energy. As these mechanisms accumulate within the process zone ahead of the crack tip, the damage becomes less localised, and both the size and number of events increase. This could explain the gradual rise in released energy until a critical damage state is reached, at which point damage coalescence triggers a sudden increase in crack length and a reduction in process-zone size, consistent with the previously described crack-jump behaviour. It must be noted that acoustic energy measurements can only be considered a qualitative and statistical descriptor of damage accumulation. In many cases, no clear trend consistent with the observed process zone growth is identified. For $R = 0.1$, different damage coalescence mechanisms and process zone growth events likely occur within a single analysed segment, preventing the emergence of a clear trend. In addition, isolated high-energy outlier signals can bias the observation of overall damage accumulation trends.

### 3.4. Fractographic analysis

The SEM images presented in Fig. 13 were used to analyse the fracture surface from various Mode II fatigue fracture surfaces at different R-ratios.

Across all specimens, the predominant fracture features are fibre pull-out, fibre surface exposure, and fibre imprints, indicating that crack growth primarily occurred along the fibre/matrix interface (i.e. delamination). In resin-rich regions, distinct cusp formations are observed, which are commonly reported as morphological markers of shear-driven crack propagation [50]. The alignment and inclination of these cusps provide a clear indication of the fracture direction and the local shear deformation mechanisms active during delamination growth.

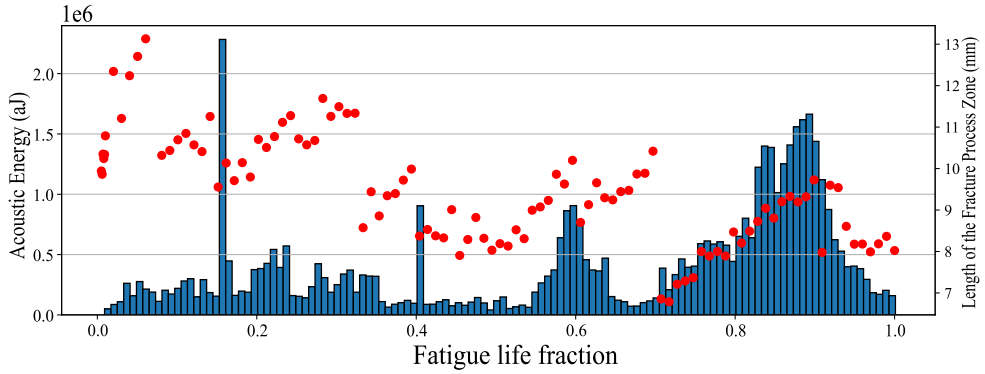


**Fig. 11.** Histogram for release of acoustic energy (left axis) during fatigue test at $R = 0.3$ compared with the process zone length evaluated with DIC (red circles, right axis).

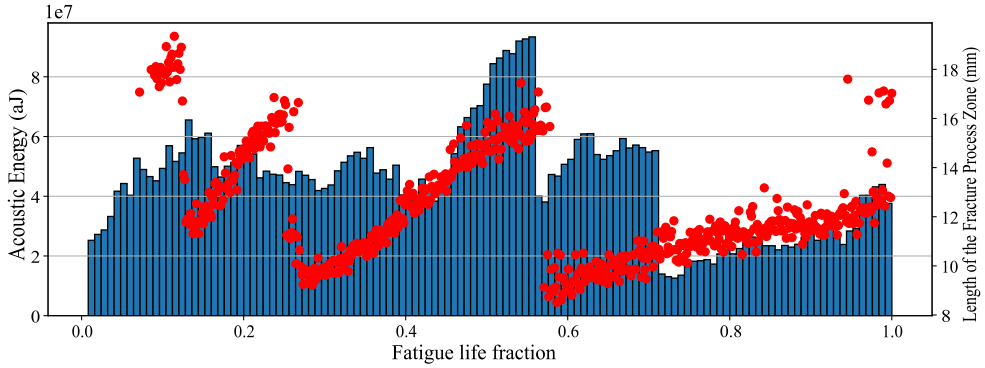


**Fig. 12.** Histogram for release of acoustic energy (left axis) during fatigue test at $R = 0.5$ compared with the process zone length evaluated with DIC (red circles, right axis).

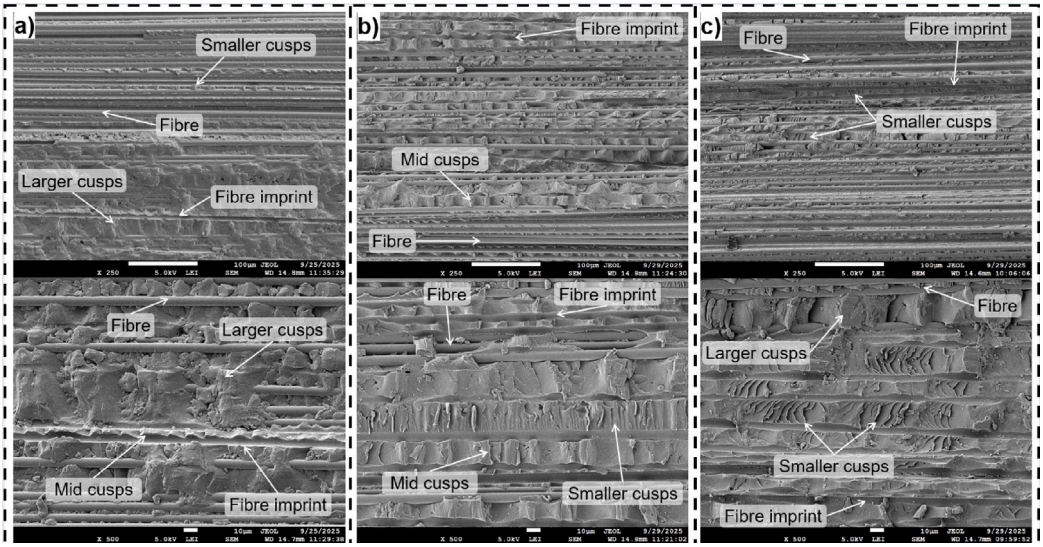


**Fig. 13.** SEM micrographs of the Mode II fatigue fracture surfaces obtained at different R-ratios where the crack propagated from left to right. (a) $R = 0.1$, (b) $R = 0.3$, and (c) $R = 0.5$. The top row (250×) provides an overall view of the fracture morphology, while the bottom row (500×) highlights the finer details of the failure features.

A comparative inspection reveals that as the R-ratio increases, the average cusp spacing decreases. Larger cusps are evident in the specimen tested at $R = 0.1$ (Fig. 13a), whereas shorter cusps dominate at $R = 0.5$ (Fig. 13c). These findings are consistent with the fractographic observations of Amaral et al. [16], who reported similar effects in Mode II fatigue propagation. The authors suggested that the amplitude of the applied load influences the formation and size of cusps. The intermediate case ($R = 0.3$, Fig. 13b) exhibits transitional morphology, with moderately spaced cusps and partially deformed cusp tips. This indicates the onset of local plastic deformation and micro-rolling effects, caused by increased interfacial friction between the opposing fracture surfaces.

Furthermore, the height and sharpness of cusp peaks also vary with the R-ratio. At $R = 0.1$ (Fig. 13a), the cusps appear lower and less

defined, making it difficult to distinguish between debris and cusps. This suggests an increase in frictional interaction after crack propagation, which could alter traditional fracture patterns. In contrast, the specimen tested at R = 0.5 (Fig. 13c) has more pronounced and closely spaced cusps, which indicate reduced interfacial friction after propagation. The specimen tested at R = 0.3 (Fig. 13b) has deformed or rolled cusp tips, which may have been caused by repeated sliding contact between the fractured surfaces during cyclic loading. These friction-induced morphological alterations are significant because they affect local energy dissipation mechanisms and influence the mechanical response to continued shear fatigue loading.

Overall, these observations confirm that the Mode II fatigue delamination morphology evolves systematically with the R-ratio, reflecting the interplay between matrix shear deformation, fibre/matrix interfacial strength, and the frictional effects that become less dominant at higher R values. In other words, the lower R-ratio ($R = 0.1$) may induce a larger relative sliding between the adherends during cyclic loading. This sliding promotes intermittent contact and local friction between the opposing fracture surfaces, particularly near the crack front. Such frictional interactions can alter the cusp morphology by flattening or partially rolling their tips, as observed in Fig. 13a. Conversely, at higher load ratios ($R = 0.5$), the smaller load amplitude reduces bending and limits the extent of frictional modification, resulting in smaller and more defined cusps.

Furthermore, the observations are in good agreement with the AE analysis discussed in Section 3.3. For the higher R-ratios ($R = 0.3$ and $R = 0.5$), the cumulative AE energy exhibits a progressive build-up followed by abrupt releases, indicating that damage within the FPZ accumulates until relatively high values of energy are reached, at which point coalescence of microcracks and cusps triggers crack-jump events. The finer and more densely distributed cusps observed at $R = 0.5$ are consistent with these frequent, localised coalescence events. In contrast, at the lower R-ratio ($R = 0.1$), the AE response is more scattered and does not show a clear monotonic build-up of energy, which is in line with the presence of larger, more worn and widely spaced cusps.

The combined DIC, AE and fractographic evidence supports a consistent damage-progression mechanism under Mode II fatigue: the FPZ grows through microcracking and cusp formation until local coalescence events trigger crack jumps. The characteristic cusp morphology at each R-ratio therefore provides a post-mortem signature of the underlying FPZ evolution and crack-jump behaviour inferred from the AE and DIC measurements.

## 4. Conclusions

Mode II fatigue delamination at various R-ratios was investigated using the End-Loaded Split (ELS) specimen configuration. A multi-method experimental approach was employed to characterise the development of the Fracture Process Zone (FPZ), combining Digital Image Correlation (DIC), Acoustic Emissions (AE) and post-mortem fractography analysis.

The true and effective crack lengths were independently determined from DIC strain measurements taken from the side (2D) and top (3D) of the tested specimens, respectively. Although each of the DIC methods presented specific limitations, their combined use enabled the identification of the FPZ. In this framework, the effective crack length reflects the region over which microcracking and cusp formation occur ahead of the delamination front (at FPZ), whereas the true crack length (delamination tip) marks the point at which these features eventually coalesce.

The length of the fracture process zone was found to evolve during fatigue delamination, rather than remaining constant. This behaviour was attributed to the varying rates at which the underlying fracture mechanisms develop. Microcracking and cusp formation gradually extend the FPZ (measured here as effective crack length), while cusp coalescence events lead to sudden advances of the crack tip, referred to as ‘crack jumps’ (measured here as true crack length). This resulted in a temporary reduction of the FPZ length before delamination growth was resumed.

The evolution of the FPZ was influenced by the R-ratio. At higher R-ratios, in most cases, the cyclic loading led to a greater accumulation of energy within the FPZ prior to coalescence. This behaviour was accompanied by fluctuations in the length of the FPZ. In contrast, at lower R-ratios, increased interfacial friction dissipated a larger fraction of the input energy, resulting in less pronounced oscillations of the FPZ’s length and a more gradual delamination growth.

Fractographic observations further supported these findings. Lower R-ratios were associated with larger, more widely spaced cusps and evidence of enhanced frictional wear, whereas higher R-ratios produced finer, more sharply defined cusps. These morphological signatures are consistent with the distinct FPZ development and energy dissipation mechanisms inferred from the DIC and AE analyses.

Overall, the results demonstrate that Mode II fatigue delamination is governed by the interplay between FPZ evolution, frictional sliding and crack-tip coalescence, which are strongly influenced by the applied R-ratio. These insights contribute to a mechanistic understanding of shear-driven fatigue crack growth and may support improved modelling and structural durability assessment of composite laminates.

## CRediT authorship contribution statement

**Johan Birnie:** Writing – review & editing, Writing – original draft, Visualization, Investigation, Formal analysis, Data curation, Conceptualization. **Davide Biagini:** Writing – review & editing, Writing – original draft, Visualization, Formal analysis, Data curation. **Maria Pia Falaschetti:** Writing – review & editing, Validation, Supervision, Methodology. **Francisco Monticeli:** Writing – review & editing, Writing – original draft, Formal analysis. **John-Alan Pascoe:** Writing – review & editing, Supervision, Resources. **Enrico Troiani:** Writing – review & editing, Supervision, Resources, Funding acquisition.

## Declaration of competing interest

The authors declare that they have no known competing financial interests or personal relationships that could have appeared to influence the work reported in this paper.

## Acknowledgements

This research was financed by the European Union—NextGenerationEU through the Italian Ministry of University and Research under PNRR—Mission 4 Component 1, Investment 4.1 “Extension of the number of PhD programmes and innovative PhD programmes for Public Administration and cultural heritage” and Investment 3.4 “Advanced university education and skills–Support to PhD programmes for digital and environmental transition” (CUP: J33C23002650002).

## Data availability

The data underlying this work is publicly available via a Zenodo repository: https://doi.org/10.5281/zenodo.18640627.

## References

[1] Zhang J, Lin G, Vaidya U, Wang H. Past, present and future prospective of global carbon fibre composite developments and applications. Compos B: Eng 2023;250:110463. http://dx.doi.org/10.1016/j.compositesb.2022.110463, URL https://www.sciencedirect.com/science/article/pii/S1359836822008368.

[2] Wisnom MR. The role of delamination in failure of fibre-reinforced composites. Philos Trans R Soc A: Math Phys Eng Sci 2012;370(1965):1850–70. http://dx.doi.org/10.1098/rsta.2011.0441, URL https://royalsocietypublishing.org/doi/10.1098/rsta.2011.0441.

[3] Greenhalgh ES. 4 - delamination-dominated failures in polymer composites. In: Failure analysis and fractography of polymer composites. Woodhead publishing series in composites science and engineering, Cambridge: Woodhead Publishing; 2009, p. 164–237. http://dx.doi.org/10.1533/9781845696818.164, URL https://www.sciencedirect.com/science/article/pii/B9781845692179500044.

[4] ASTM D7905:2014. Standard test method for determination of the mode II interlaminar fracture toughness of unidirectional fiber-reinforced polymer matrix composites. 2014, West Conshohocken, PA, USA. URL https://doi.org/10.1520/D7905_D7905M-19E01.

[5] Russell AJ, Street KN. Factors affecting the interlaminar fracture energy of graphite/epoxy laminates. In: Progress in science and engineering of composites. Tokyo; 1982, p. 279–86, URL https://cir.nii.ac.jp/crid/1573387449040385408.

[6] Carlsson L, GillespieJR J, Pipes R. On the analysis and design of the end notched flexure (ENF) specimen for mode II testing. J Compos Mater 1986;20(6):594–604. http://dx.doi.org/10.1177/002199838602000606.

[7] ISO. ISO 15114:2014(E): Fibre-reinforced plastic composites—determination of the mode II fracture resistance for unidirectionally reinforced materials using the calibrated end-loaded split (c-ELS) test and an effective crack length approach. 2014, Geneva, Switzerland.

[8] Blackman BRK, Brunner AJ, Williams JG. Mode II fracture testing of composites: a new look at an old problem. Eng Fract Mech 2006;73(16):2443–55. http://dx.doi.org/10.1016/j.engfracmech.2006.05.022, URL https://www.sciencedirect.com/science/article/pii/S0013794406002086.

[9] Wilk J. Applicability of mode II interlaminar fracture toughness testing methods for characterization of thermoplastic laminates with woven fabric reinforcements. Eng Fract Mech 2019;216:106533. http://dx.doi.org/10.1016/j.engfracmech.2019.106533, URL https://www.sciencedirect.com/science/article/pii/S0013794418314334.

[10] European Union Aviation Safety Agency (EASA). AMC 20-29: Composite aircraft structure. 2010, URL https://www.easa.europa.eu/en/downloads/1698/en.

[11] Russell A, Street K. The effect of matrix toughness on delamination: Static and fatigue fracture under mode II shear loading of graphite fiber composites. In: Johnston N, editor. Toughened composites. vol. STP937-EB, ASTM International; 1987, http://dx.doi.org/10.1520/STP24383S.

[12] Martin R, Murri G. Characterization of mode I and mode II delamination growth and thresholds in AS4/PEEK composites. In: Garbo S, editor. Composite materials: Testing and design (ninth volume). vol. STP1059-EB, ASTM International; 1990, http://dx.doi.org/10.1520/STP24115S.

[13] Tanaka K, Tanaka H. Stress-ratio effect on mode II propagation of interlaminar fatigue cracks in graphite/epoxy composites. In: Armanios E, editor. Composite materials: Fatigue and fracture (sixth volume). vol. STP1285-EB, ASTM International; 1997, http://dx.doi.org/10.1520/STP19925S.

[14] Matsubara G, Ono H, Tanaka K. Mode II fatigue crack growth from delamination in unidirectional tape and satin-woven fabric laminates of high strength GFRP. Int J Fatigue 2006;28(10):1177–86. http://dx.doi.org/10.1016/j.ijfatigue.2006.02.006, URL https://www.sciencedirect.com/science/article/pii/S0142112306000387.

[15] Hojo M, Ando T, Tanaka M, Adachi T, Ochiai S, Endo Y. Modes I and II interlaminar fracture toughness and fatigue delamination of CF/epoxy laminates with self-same epoxy interleaf. Int J Fatigue 2006;28(10):1154–65. http://dx.doi.org/10.1016/j.ijfatigue.2006.02.004, URL https://www.sciencedirect.com/science/article/pii/S0142112306000351.

[16] Amaral L, Zarouchas D, Alderliesten R, Benedictus R. Energy dissipation in mode II fatigue crack growth. Eng Fract Mech 2017;173:41–54. http://dx.doi.org/10.1016/j.engfracmech.2017.01.020, URL https://www.sciencedirect.com/science/article/pii/S0013794416304787.

[17] Lee SM. Mode II delamination failure mechanisms of polymer matrix composites. J Mater Sci 1997;32(5):1287–95. http://dx.doi.org/10.1023/A:1018552506085.

[18] Wang C, Vassilopoulos AP, Keller T. Experimental investigation of two-dimensional Mode-II delamination in composite laminates. Compos A: Appl Sci Manuf 2023;173:107666. http://dx.doi.org/10.1016/j.compositesa.2023.107666, URL https://www.sciencedirect.com/science/article/pii/S1359835X23002427.

[19] Salviato M, Kirane K, Bažant ZP, Cusatis G. Mode I and II interlaminar fracture in laminated composites: A size effect study. J Appl Mech 2019;86(091008). http://dx.doi.org/10.1115/1.4043889.

[20] Pérez-Galmés M, Renart J, Sarrado C, Costa J. Suitable specimen dimensions for the determination of mode II fracture toughness of bonded joints by means of the ELS test. Eng Fract Mech 2018;202:350–62. http://dx.doi.org/10.1016/j.engfracmech.2018.07.039, URL https://www.sciencedirect.com/science/article/pii/S0013794418301498.

[21] Blackman BRK, Kinloch AJ, Paraschi M. The determination of the mode II adhesive fracture resistance, *G*IIC, of structural adhesive joints: An effective crack length approach. Eng Fract Mech 2005;72(6):877–97. http://dx.doi.org/10.1016/j.engfracmech.2004.08.007, URL https://www.sciencedirect.com/science/article/pii/S0013794404001961.

[22] Naufal MI, Wong KJ, Israr HA, Nejad AF, Rahimian Koloor SS, Gan KW, Faizi MK, Siebert G. Digital image correlation technique for failure and crack propagation of fibre-reinforced polymer composites – a review. Compos Adv Mater 2024;33:26349833241253619. http://dx.doi.org/10.1177/26349833241253619.

[23] Chandra V, Chakraborty P. Automated crack extension measurement method for fracture and fatigue analysis using digital image correlation. Eng Fract Mech 2024;305:110182. http://dx.doi.org/10.1016/j.engfracmech.2024.110182, URL https://www.sciencedirect.com/science/article/pii/S001379442400345X.

[24] Murray BR, Fonteyn S, Carrella-Payan D, Kalteremidou K-A, Cernescu A, Van Hemelrijck D, Pyl L. Crack tip monitoring of mode I and mode II delamination in CF/epoxies under static and dynamic loading conditions using digital image correlation. Proceedings 2018;2(8):389. http://dx.doi.org/10.3390/ICEM18-05225, URL https://www.mdpi.com/2504-3900/2/8/389.

[25] Bernaert JVA, Calabrese AS, Botsis J, Vassilopoulos AP. Automated crack propagation detection in adhesively bonded composite joints with digital image correlation techniques. Compos B: Eng 2026;310:113113. http://dx.doi.org/10.1016/j.compositesb.2025.113113, URL https://www.sciencedirect.com/science/article/pii/S1359836825010297.

[26] Cardoso D, Pereira R, Moura M, Correia N. Assessment of fracture process zone length in carbon fiber-reinforced epoxy composites through digital image correlation. Theor Appl Fract Mech 2025;136:104816. http://dx.doi.org/10.1016/j.tafmec.2024.104816, URL https://www.sciencedirect.com/science/article/pii/S0167844224005664.

[27] Deng L, Liu L, Pascoe J-A, Alderliesten R. Experimental investigation of the effect of interface angle on mode-I fracture toughness in DCB laminates using digital image correlation. Eng Fract Mech 2025;319:110988. http://dx.doi.org/10.1016/j.engfracmech.2025.110988, URL https://www.sciencedirect.com/science/article/pii/S0013794425001894.

[28] Zhu M, Gorbatikh L, Fonteyn S, Van Hemelrijck D, Pyl L, Carrella-Payan D, Lomov SV. Digital image correlation assisted characterization of Mode I fatigue delamination in composites. Compos Struct 2020;253:112746. http://dx.doi.org/10.1016/j.compstruct.2020.112746, URL https://www.sciencedirect.com/science/article/pii/S0263822320326726.

[29] Mehrabi M, Martulli LM, Bernasconi A, Carboni M. Estimating crack tip position in adhesively bonded joints subjected to mode II quasi-static loading. Fatigue Fract Eng Mater Struct 2024;47(4):1262–80. http://dx.doi.org/10.1111/ffe.14237, _eprint: https://onlinelibrary.wiley.com/doi/pdf/10.1111/ffe.14237. URL https://onlinelibrary.wiley.com/doi/abs/10.1111/ffe.14237.

[30] Khudiakova A, Grasser V, Blumenthal C, Wolfahrt M, Pinter G. Automated monitoring of the crack propagation in mode I testing of thermoplastic composites by means of digital image correlation. Polym Test 2020;82:106304. http://dx.doi.org/10.1016/j.polymertesting.2019.106304, URL https://www.sciencedirect.com/science/article/pii/S014294181931935X.

[31] Tu W, Pascoe J-A, Alderliesten R. Comparison of mode II delamination behaviours in multidirectional and unidirectional composite laminates. Compos B: Eng 2025;291:111941. http://dx.doi.org/10.1016/j.compositesb.2024.111941, URL https://www.sciencedirect.com/science/article/pii/S1359836824007534.

[32] Saeedifar M, Zarouchas D. Damage characterization of laminated composites using acoustic emission: A review. Compos B: Eng 2020;195:108039. http://dx.doi.org/10.1016/j.compositesb.2020.108039, URL https://www.sciencedirect.com/science/article/pii/S1359836819365096.

[33] Ferreira Motta Jr R, Alderliesten R, Yutaka Shiino M, Odila Hilário Cioffi M, Jacobus Cornelis Voorwald H. Scrutinizing interlaminar fatigue loading cycle in composites using acoustic emission technique: Stress ratio influence on damage formation. Compos A: Appl Sci Manuf 2020;138:106065. http://dx.doi.org/10.1016/j.compositesa.2020.106065, URL https://www.sciencedirect.com/science/article/pii/S1359835X20303043.

[34] Falaschetti MP, Rondina F, Zavatta N, Troiani E, Donati L. Effective implementation of numerical models for the crashworthiness of composite laminates. Eng Fail Anal 2024;160:108196. http://dx.doi.org/10.1016/j.engfailanal.2024.108196, URL https://www.sciencedirect.com/science/article/pii/S1350630724002425.

[35] Birnie J, Falaschetti MP, Semprucci F, Troiani E, Birnie J, Falaschetti MP, Semprucci F, Troiani E. Experimental and numerical study of mode II fatigue delamination via end-loaded split specimens. Eng Proc 2026;119(1). http://dx.doi.org/10.3390/engproc2025119050, Company: Multidisciplinary Digital Publishing Institute Distributor: Multidisciplinary Digital Publishing Institute Institution: Multidisciplinary Digital Publishing Institute Label: Multidisciplinary Digital Publishing Institute. URL https://www.mdpi.com/2673-4591/119/1/50.

[36] Simon I, Banks-Sills L, Fourman V. Mode I delamination propagation and *R*-ratio effects in woven composite DCB specimens for a multi-directional layup. Int J Fatigue 2017;96:237–51. http://dx.doi.org/10.1016/j.ijfatigue.2016.12.005, URL https://www.sciencedirect.com/science/article/pii/S0142112316304121.

[37] Stelzer S, Brunner AJ, Argüelles A, Murphy N, Cano GM, Pinter G. Mode I delamination fatigue crack growth in unidirectional fiber reinforced composites: Results from ESIS TC4 round-robins. Eng Fract Mech 2014;116:92–107. http://dx.doi.org/10.1016/j.engfracmech.2013.12.002, URL https://www.sciencedirect.com/science/article/pii/S0013794413003858.

[38] Rans C, Alderliesten R, Benedictus R. Misinterpreting the results: How similitude can improve our understanding of fatigue delamination growth. Compos Sci Technol 2011;71(2):230–8. http://dx.doi.org/10.1016/j.compscitech.2010.11.010, URL https://www.sciencedirect.com/science/article/pii/S0266353810004495.

[39] Brunner AJ, Blackman BRK, Williams JG. Calculating a damage parameter and bridging stress from GIC delamination tests on fibre composites. Compos Sci Technol 2006;66(6):785–95. http://dx.doi.org/10.1016/j.compscitech.2004.12.040, URL https://www.sciencedirect.com/science/article/pii/S0266353804003574.

[40] de Moura MFSF, de Morais AB. Equivalent crack based analyses of ENF and ELS tests. Eng Fract Mech 2008;75(9):2584–96. http://dx.doi.org/10.1016/j.engfracmech.2007.03.005, URL https://www.sciencedirect.com/science/article/pii/S0013794407001063.

[41] Shi CN, Xu W. A double compliances method for determination of the ELS mode II interlaminar fracture toughness without measuring the growing crack length. Theor Appl Fract Mech 2024;133:104543. http://dx.doi.org/10.1016/j.tafmec.2024.104543, URL https://www.sciencedirect.com/science/article/pii/S0167844224002921.

[42] Corleto C, Bradley W, Henriksen M. Correspondence between stress fields and damage zones ahead of crack tip of composites under mode I and mode II delamination. In: Proceedings, sixth international conference on composite materials. ICCM VI, Vol. 3, London, England; 1987, p. 378–87.

[43] Massabo R, Cox BN. Concepts for bridged Mode ii delamination cracks. J Mech Phys Solids 1999;47(6):1265–300. http://dx.doi.org/10.1016/S0022-5096(98)00107-0, URL https://www.sciencedirect.com/science/article/pii/S0022509698001070.

[44] Xing H, Xie F, Wang M, Xie K, Qiu Y. Experimental investigation of fracture process zone of rock in dynamic mode I fracturing and its effect on dynamic crack initiation toughness. Eng Fract Mech 2022;275:108828. http://dx.doi.org/10.1016/j.engfracmech.2022.108828, URL https://www.sciencedirect.com/science/article/pii/S001379442200546X.

[45] Falcetelli F, Cristiani D, Yue N, Sbarufatti C, Troiani E, Di Sante R, Zarouchas D. Qualification of distributed optical fiber sensors using probability of detection curves for delamination in composite laminates. Struct Health Monit 2023;22(5):2972–86. http://dx.doi.org/10.1177/14759217221141159.

[46] Cristiani D, Falcetelli F, Yue N, Sbarufatti C, Di Sante R, Zarouchas D, Giglio M. Strain-based delamination prediction in fatigue loaded CFRP coupon specimens by deep learning and static loading data. Compos B: Eng 2022;241:110020. http://dx.doi.org/10.1016/j.compositesb.2022.110020, URL https://www.sciencedirect.com/science/article/pii/S1359836822003985.

[47] Sourisseau Q, Lepretre E, Chataigner S, Chapeleau X, Mouton L, Paboeuf S. Use of high spatial resolution distributed optical fiber to monitor the crack propagation of an adhesively bonded joint during ENF and DCB tests. Int J Adhes Adhes 2022;115:103124. http://dx.doi.org/10.1016/j.ijadhadh.2022.103124, URL https://www.sciencedirect.com/science/article/pii/S0143749622000410.

[48] Panerai A, Martulli LM, Bernasconi A, Carboni M. Advanced strain-based approaches for monitoring crack tip position in adhesively bonded joints subjected to mixed mode fatigue loading. Int J Fatigue 2025;197:108946. http://dx.doi.org/10.1016/j.ijfatigue.2025.108946, URL https://www.sciencedirect.com/science/article/pii/S0142112325001434.

[49] Allegri G, Jones MI, Wisnom MR, Hallett SR. A new semi-empirical model for stress ratio effect on mode II fatigue delamination growth. Compos A: Appl Sci Manuf 2011;42(7):733–40. http://dx.doi.org/10.1016/j.compositesa.2011.02.013, URL https://www.sciencedirect.com/science/article/pii/S1359835X11000571.

[50] Mohammadi R, Najafabadi MA, Saghafi H, Saeedifar M, Zarouchas D. The effect of mode II fatigue crack growth rate on the fractographic features of CFRP composite laminates: An acoustic emission and scanning electron microscopy analysis. Eng Fract Mech 2021;241:107408. http://dx.doi.org/10.1016/j.engfracmech.2020.107408, URL https://www.sciencedirect.com/science/article/pii/S001379442030984X.